

# Simulation and Experimental Analyses on Quasi-Static and Dynamic Performances of Four-Star Cellular Structure

Ying ZHAO\*, Yu CHEN, Songchuan ZHENG, Jusan YIN, Jinyu SHI, Yunwu LI

**Abstract:** A novel four-star cellular structure (FSCS) is proposed. Firstly, relative density of FSCS, regular octagons and regular hexagons are obtained accordingly. Then, their in-plane quasi-static and dynamic performances are conducted under the premise of equal number of cells, equal mass and equal relative density by adopting Hyperworks and Ls-Dyna software. Macroscopic deformation processes indicate that FSCS, regular octagons and regular hexagons are presented as "compression-shrinkage" negative Poisson's ratio deformation mode, "V" deformation mode and "X" deformation mode, respectively. Subsequently, size effects of unit cell are carried out, and as the number of cell layers reaches no less than 9, platform stress of FSCS gradually tends to be stable. To verify the accuracy of finite element (FE) simulation models, quasi-static compression test is executed on three-dimensional FSCS. The results indicate that FE simulation results agree well with experimental predictions, and the proposed FSCS is equipped with superior energy absorption capability.

**Keywords:** FE simulation analysis; four-star cellular structure; negative Poisson's ratio; quasi-static and dynamic performances; test verification

## 1 INTRODUCTION

Honeycomb structures have been widely studied in the fields of aerospace, automobile, and navigation owing to their excellent properties including high specific stiffness and strength, low volume consumable ratio, excellent fatigue stability, impact resistance and thermal insulation [1-2]. And it commonly includes regular hexagons, concave hexagons, rhombus, regular quadrilateral, circle, star, arrow, etc. [3-4].

The pioneering researches mostly focus on honeycomb structures with the characteristic of positive Poisson's ratio (PPR), but these materials are more fragile than those of negative Poisson's ratio (NPR) with respect to impact resistance or tolerance [5-6]. With the deepening of research, honeycomb structures with NPR characteristic have attracted more and more attention due to their unique mechanical properties. NPR materials shrink when compressed, resulting in higher fracture toughness, impact resistance, explosion resistance, and indentation hardness [7-8].

As for mechanical performances of NPR cellular structures, mechanical properties including collapse stress, yield stress and platform stress were always acquired through finite element (FE) analysis under the conditions of quasi-static and dynamic compression. Lu Z. X. et al. carried out analytical and FE simulations to obtain the in-plane Poisson's ratio and Young's modulus of a novel concept of structure with honeycomb-like configuration under uniaxial loading [9]. Fu M. H. et al. investigated a novel honeycomb by embedding rhombic configuration into normal re-entrant hexagonal honeycomb in order to enhance its in-plane mechanical properties, and analytical expressions of equivalent Young's modulus and Poisson's ratio were also deduced by adopting beam theory [10]. Shen J. B. et al. put forward a novel NPR structure containing curved re-entrant sides and dynamic behaviors were studied with the adoption of FE approach, and the results indicated that this NPR structure was equipped with outstanding energy absorption capacity compared with other structures with arc angles [11]. Zhang X. C. et al. analyzed in-plane dynamic crushing behaviors and energy-absorbed characteristics of NPR honeycombs by means of

explicit dynamic finite element analysis [12]. Qi C. et al. studied in-plane crushing responses of tetra-chiral honeycombs under both quasi-static and dynamic loading conditions [13]. Zhang J. et al. explored the dynamic tensile behavior of an auxetic structure with representative re-entrant topology [14].

The above pioneering studies have provided guidance and foundation for further research on mechanical performances of other novel NPR structures, while experimental verification and deformation modes in various impact velocities are ignored, and performance comparisons with conventional PPR honeycomb structures are not considered either. To sum up, a novel four-star cellular structure (FSCS) is put forward in this paper, as presented in Fig. 1a. Firstly, the relative density expressions of architected cellular structures (ACS) including FSCS, regular octagon honeycomb (ROH) and regular hexagon honeycomb (RHH) are derived. Secondly, macro-structural responses and micro-deformation patterns of FSCS, ROH and RHH under quasi-static compression and dynamic impact loadings with the conditions of equal relative density, equal cell number and equal mass are analyzed through FE simulation method based on the theory of shock wave propagation. Thirdly, FE simulation analysis method is utilized to analyze the influences of various layers of cells on their mechanical performances. Finally, quasi-static compression test is executed on three-dimensional (3D) FSCS sample in order to verify the accuracy of FE simulation analysis.

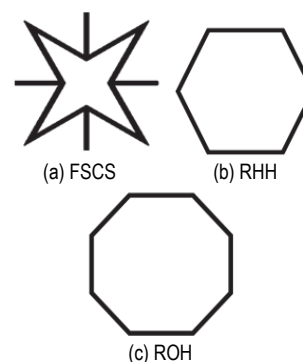


Figure 1 Three different configurations of ACS

**2 RELATIVE DENSITY**

In order to conduct the quasi-static and dynamic simulation analyses smoothly, and compare the macroscopic impact deformation processes of the three ACS, the establishment of relative density theoretical model is essential. Hence, analytical expressions of relative density of the three sorts of ACS are derived as follows.

The unit cell of re-entrant octagon is formed by the indentation of four vertices of regular octagonal honeycomb or four sides of square, connecting with other unit cells through four ribs. The corresponding ACS is connected by a certain number of re-entrant octagon cells through four reinforcing bars and arranged periodically along the X-axis and Y-axis, as exhibited in Fig. 2. According to homogenization theory [15], boundary issues can be decomposed into unit cell problem and structural problem by means of homogenization theory based on consistency assumption of microscopic periodicity and unit cell domain. Quasi-static and dynamic mechanical performances of the whole cellular structure can be described by representative unit cell accurately, including relative density, elastic modulus, plateau stress, unit volume energy absorption etc. Hence, the unit cell is taken as research object to obtain relative density of cellular structure herein, and there is no need to consider the interactions between unit cells.

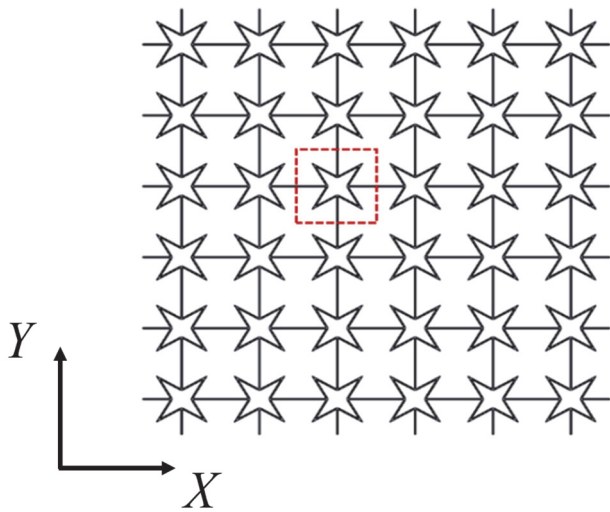


Figure 2 6 × 6 FSCS

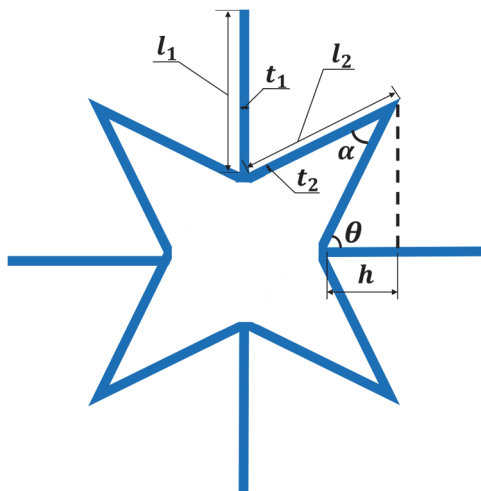


Figure 3 Structural parameters of unit cell

It can be seen from Fig. 3 that the FSCS is determined by several structural parameters and variables, consisting of length of stiffener  $l_1$ , in-plane thickness of reinforced rib  $t_1$ , re-entrant distance  $h$ , distance  $T$  perpendicular to 2D plane, length  $l_2$  and thickness  $t_2$  of eight reinforcing bars. Among which, the angle between re-entrant edge and horizontal reinforcing rib is represented as  $\theta$ , and the angle between upper and lower re-entrant edges and left and right re-entrant edges is  $\alpha$ , and  $\alpha = 2\theta - 90^\circ$ ,  $\theta \in (45^\circ, 90^\circ)$ .

According to porous material theory [16], relative density  $\rho_{NA-2D}$  of re-entrant octagon can be expressed as the ratio of density of ACS to matrix material constructing the FSCS, that is,  $\rho_{NA-2D} = \rho^* / \rho_s$ , where,  $\rho^*$  refers to density of FSCS, and  $\rho_s$  represents density of matrix material utilized by ACS.

If 2D re-entrant octagon is stretched to a certain thickness  $T$  along Z-axis,  $\rho_{NA-2D}$  can also be represented by the ratio of solid area of representative unit cell to cross-sectional area of entire cell. Since the re-entrant octagon keeps symmetrical up and down, left and right at the center, the relative density  $\rho_{NA-2D}$  can also be converted to the ratio of solid structure area of 1/4 unit cell to cross-section area of 1/4 unit cell. The equivalent relative density  $\rho_{NA-2D}$  can be given by:

$$\rho_{NA-2D} = \frac{S_s}{S_w} = \frac{l_1 t_1 + 2 l_2 t_2}{\left[ l_1 + l_2 (\sin \theta - \cos \theta) + \frac{1}{2} t_1 \right]^2} \tag{1}$$

Among which,  $S_s$  represents area of 1/4 unit cell wall,  $S_w$  refers to total area of 1/4 unit cell. Assuming that the length coefficient of re-entrant edge is  $a = l_2 / l_1$ , in-plane thickness coefficient of re-entrant edge is  $b = t_2 / l_2$ , in-plane thickness coefficient of reinforced rib can be expressed as  $c = t_1 / l_1$ , re-entrant degree can be described as  $d = h / l_1$ , out-plane thickness coefficient is  $T / l_1$ , and  $\sin \alpha / 2 = (\sqrt{l_2^2 - h^2} - h) / \sqrt{2} l_2$ . Hence, the equivalent relative density  $\rho_{NA-2D}$  can be converted into the following expression:

$$\rho_{NA-2D} = \frac{c + 2a^2 b}{\left( 1 + \sqrt{a^2 - d^2} - d \right)^2} \tag{2}$$

The 3D re-entrant octagon unit cell is formed by rotating 2D re-entrant octagon unit cell  $90^\circ$  around the axis formed by the upper and lower concave points and arranged along X-axis, Y-axis, and Z-axis periodically. Similarly, the relative density  $\rho_{NA-3D}$  is given by:

$$\rho_{NA-3D} = \frac{V_s}{V_w} \tag{3}$$

where,  $V_s$  stands for solid volume of 1/8 3D cell wall,  $V_w$  represents volume of 1/8 whole 3D unit cell, which can be explained as follows:

$$V_s = S_s \cdot T \tag{4}$$

and  $V_w$  is given by:

$$V_w = \left[ l_1 + l_2 (\sin \theta - \cos \theta) + \frac{1}{2} t_1 \right]^3 \tag{5}$$

Based on the above three expressions, relative density  $\rho_{NA-3D}$  of 3D FSCS is finally expressed as:

$$\begin{aligned} \rho_{NA-3D} &= \frac{T(l_1 t_1 + 2l_2 t_2)}{\left[ l_1 + l_2 (\sin \theta - \cos \theta) + \frac{1}{2} t_1 \right]^3} = \\ &= \frac{T}{l_1 + l_2 (\sin \theta - \cos \theta) + \frac{1}{2} t_1} \rho_{NA-2D} \end{aligned} \tag{6}$$

Similarly, the relative density  $\rho_{ZB-2D}$  of 2D ROH can also be obtained according to the method above. As shown in Fig. 4 and Fig. 5, in-plane arrangement of ROH and representative unit cell are demonstrated respectively. The structural parameters consist of length of edge  $l$  and thickness of edge  $t$ .

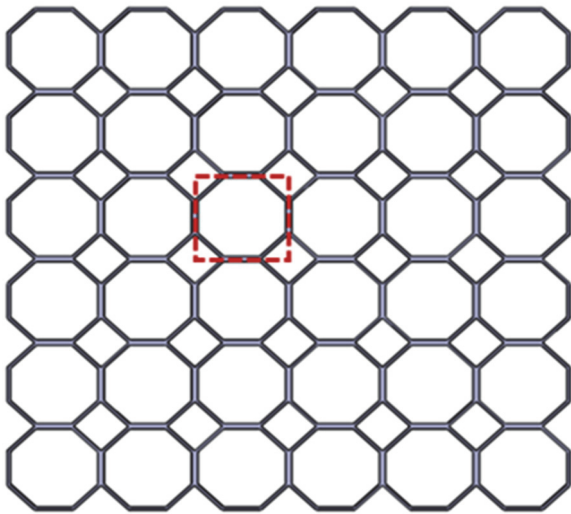


Figure 4 In-plane arrangement of 2D ROH

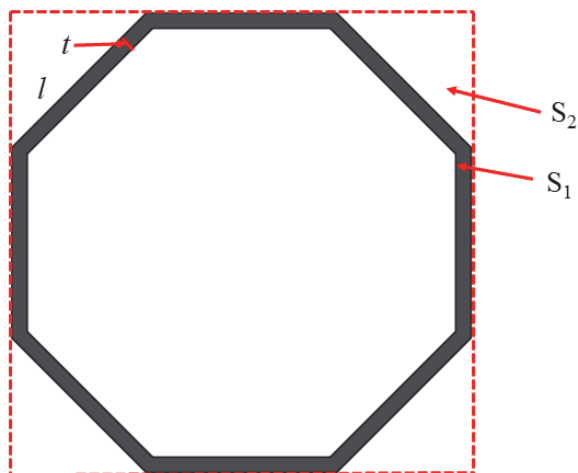


Figure 5 Representative unit cell of ROH

$$\rho_{ZB-2D} = \frac{S_1}{S_2} \tag{7}$$

Considering the structural parameters of this ROH, the relative density  $\rho_{ZB-2D}$  of 2D ROH can be given by:

$$\rho_{ZB-2D} = \frac{S_1}{S_2} = \frac{8lt - 8(\sqrt{2} - 1)t^2}{(\sqrt{2} + 1)^2 l^2} \tag{8}$$

In the same way, 2D RHH is exhibited in Fig. 6, and its structural parameters are unilateral length  $l$  and cellular thickness  $t$ . Its relative density  $\rho_{ZL-2D}$  can be given as the following Eq. (9).

$$\rho_{ZL-2D} = \frac{2}{\sqrt{3}} \frac{t}{l} \left( 1 - \frac{1}{2\sqrt{3}} \frac{t}{l} \right) \tag{9}$$

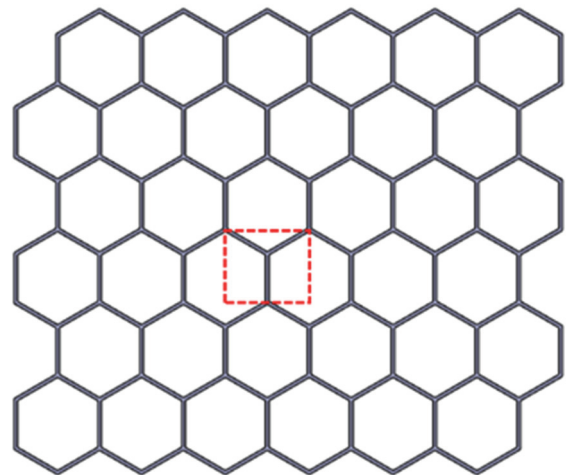


Figure 6 In-plane arrangement of 2D RHH

### 3 FE SIMULATION ANALYSIS

To analyze in-plane axial impact deformation modes and energy absorption capability of the three ACS, the corresponding FE calculation models should be established. The in-plane impact dynamic characteristics of FSCS, ROH and RHH are emulated by employing Hyperworks and Ls-Dyna software. Firstly, the three ACS are successively filled into a panel with size of  $L_1 \times L_2$ , Fig. 7 reveals the FE calculation model of ACS under in-plane impact loading.

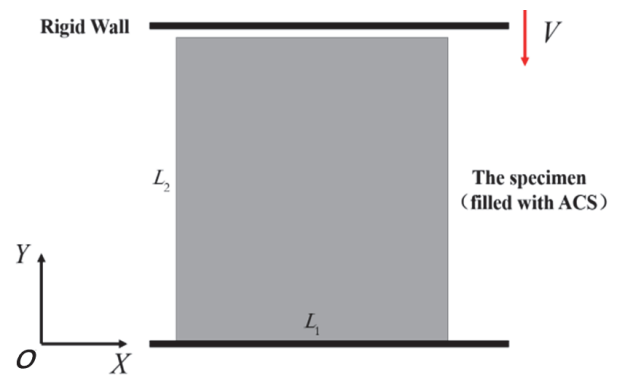


Figure 7 Computational model of ACS under in-plane impact loading

Assuming cell wall length of FSCS as  $l_1 = 20.462$  mm,  $l_2 = 24.249$  mm,  $t_1 = t_2 = 1.077$  mm,  $\theta = 60^\circ$ . On the basis of the premise of equal number of cells, equal total mass and equal relative density, the unit cell sizes of ROH and RHH can be obtained that the length and thickness of regular octagon cell wall are  $l = 24.299$  mm, and  $t = 1.680$  mm, while the same physical quantity of regular hexagonal cell wall is  $l = 33.882$ ,  $t = 1.35$  mm.

On the premise of equal cell number, the cell number of the three ACS is set as  $13 \times 13$  along  $X$ -axis and  $Y$ -axis, respectively. In accordance with the description above, FE calculation models of FSCS, ROH and RHH are established respectively, as shown in Fig. 8.

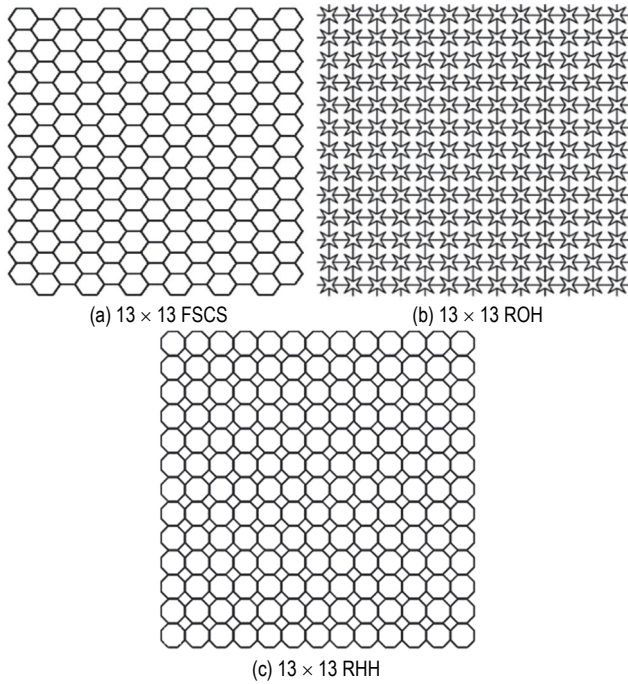


Figure 8 FE calculation models of three types of ACS with equal cell number of  $13 \times 13$

During the process of simulation, 302 stainless steel is chosen as the matrix material of the three ACS which are assumed to be elastoplastic models. Specific material parameters are exhibited in Tab. 1. The upper and lower rigid plates are both made of steel. A velocity of  $V$  is imposed on the upper rigid plate along the negative direction of  $Y$ -axis. The lower rigid plate is utilized to fix the ACS. According to the results of mesh number convergence, simultaneously allowing for calculation accuracy and computation time, the number of elements in re-entrant edge of each FSCS and cellular reinforcement rib are both kept 8. Among which, the total number of elements in FSCS keeps 18928, while in RHH and ROH keeps 65826 and 77551, respectively. Five integration points are taken along the direction of thickness to ensure convergence. In order to avoid hour glass phenomenon during the process of calculation, surface-to-surface contact is adopted between rigid plate and ACS, and static and dynamic friction factors are set as 0.2 and 0.2 respectively. While the contact among ACS cells is set as single-surface contact, and the dynamic and static friction coefficients are also set as 0.2 and 0.2 respectively. Six degrees of freedom at the bottom of the three ACS are completely constrained, with the left and right degrees of

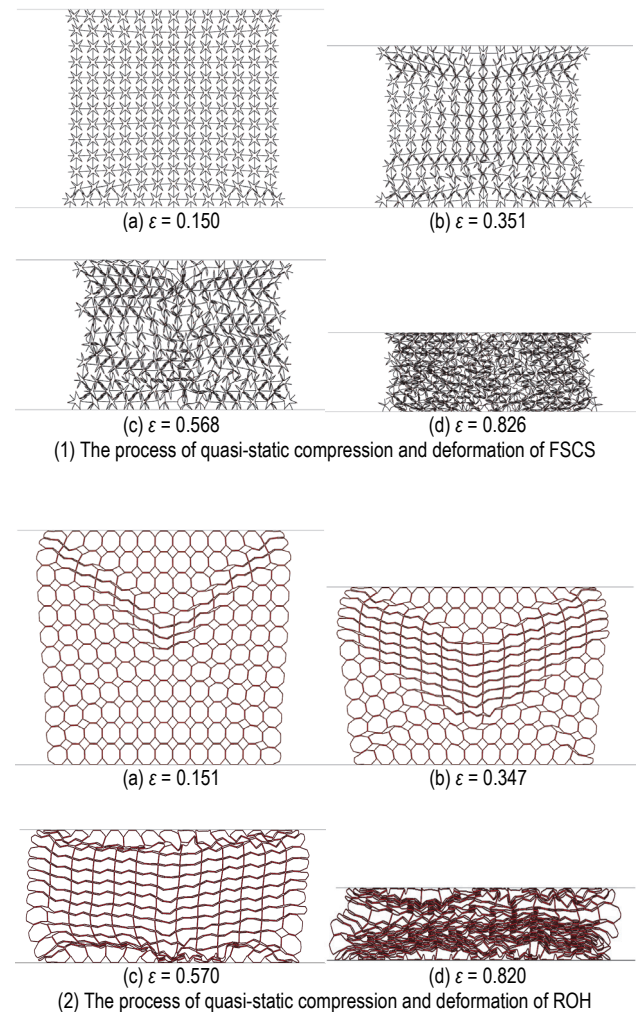
freedom released. Additionally, in order that the deformation of ACS stays in the state of in-plane strain, out-of-plane displacements of all nodes are limited and out-plane deformation is not considered herein. Equally, the out-plane thicknesses of the three FE models along  $Z$ -axis direction are executed as 1 mm.

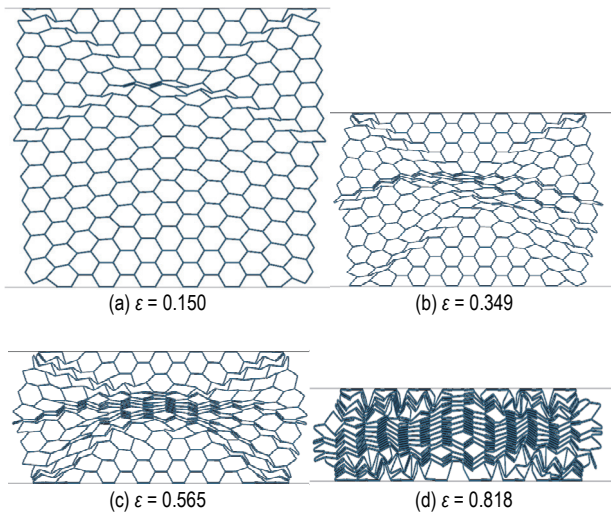
Table 1 Parameters of matrix material and rigid plate material

	Matrix Material 302 stainless steel	Rigid plate
Density, $\rho_s$ / kg/m <sup>3</sup>	7930	7850
Young's modulus, $E_s$ / GPa	194	210
Poisson's ratio, $\mu$	0.3	0.3
Yield stress, $\sigma_{ys}$ / MPa	205	/

#### 4 QUASI-STATIC COMPRESSION ANALYSIS

According to the FEA method introduced above, a velocity of 2 mm/min is applied to the upper rigid wall while the bottom rigid wall at the bottom is completely limited. Ultimately, the quasi-static compression deformation processes and quasi-static stress-strain curves of FSCS, RHH and ROH are obtained, as exhibited in Fig. 9 and Fig. 10 respectively. To observe and compare quasi-static compression deformation process of three ACS easily, the macroscopic compression deformation diagram of three ACS materials under various compression strains are also acquired.





(3) The process of quasi-static compression and deformation of RHH  
**Figure 9** Quasi-static compression and deformation of the three ACS

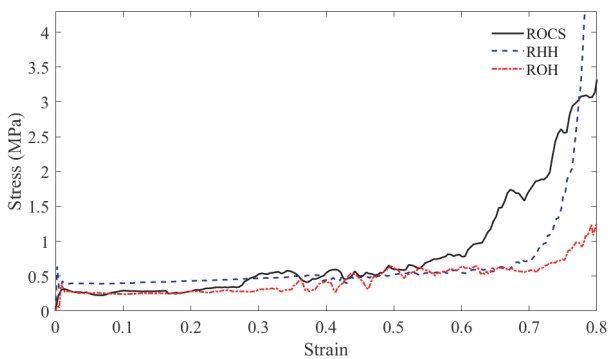


**Figure 10** Quasi-static stress-strain curves of the three ACS

As illustrated in Fig. 9, FSCS begins to demonstrate a tendency to shrink toward the middle as the compression is further enhanced, presenting an obvious "compression-contraction" NPR characteristic, while the RHH and ROH keep the PPR property of "compression-expansion" all the time. With the increase of compression, the stress of FSCS increases obviously earlier than those of RHH and ROH. It is because the NPR characteristic of FSCS forces structural material to gather into the middle and the rods to contact with each other earlier to form a new support that leads to increasing compression stress. The stresses of RHH and ROH increase evidently only when the material is compacted. It can also be demonstrated from Figure 10 that the yield stress of FSCS proves equivalent to that of ROH, since the yield stress of the three ACS is the stress formed by the bending of the rods that compose the ACS. All the introduced above indicate that FSCS exhibit more excellent capability of compression resistance compared with the other two ACS. Due to the unique deformation process and stress-strain curve representation of FSCS with NPR, the compression stress-strain curve can be divided into four areas: elastic region, platform stress region, platform stress-enhancement region and densification area. While the other two ACS are possessed with three areas composed of elastic area, platform stress area and densification area. Since the area that the stress increases owing to the NPR characteristic of "compression-contraction" is called "platform stress-enhancement area", the growth rate of the stress in platform stress-enhancement region is obviously lower than that in the compacted region

for the FSCS. Fig. 11 and Fig. 12 illustrate the divisions of the stress-strain curves of the FSCS and RHH, respectively.

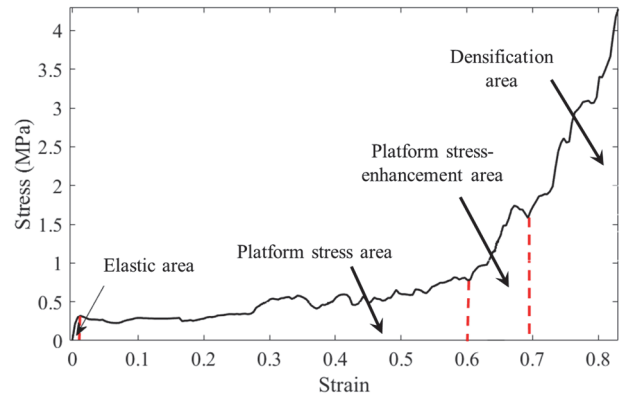


**Figure 11** Division of the stress-strain curve of FSCS with NPR

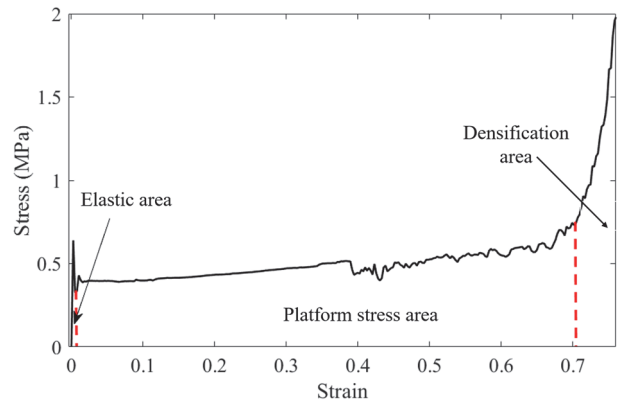


**Figure 12** Division of the stress-strain curve of RHH with PPR

The FSCS with NPR possesses a smaller slope of stress increase corresponding to specific platform stress-enhancement area, which indicates that it has higher efficiency of energy absorption.

## 5 ANALYSES ON DYNAMIC IMPACT PERFORMANCES OF SHOCK WAVE PROPAGATION THEORY

The impact end instantly generates stress and the particle gains a velocity as dynamic loading is applied to ACS. These stresses and velocities will propagate from the impact end to the other side in the form of shock wave. During the process, if the stress generated in ACS proves to be lower than the yield stress of matrix material, the strain generated and the stress wave will be both elastic. The maximum propagation speed of elastic stress wave can be indicated as follows:

$$c_L = \sqrt{\frac{E}{\rho}} \tag{10}$$

For the ACS,  $c_p$  stands for the propagation velocity of plastic wave and the yield velocity  $v_y$  is also known as trapped velocity  $V_w$ , which is given by:

$$v_y = V_w = \frac{\sigma_y}{E} c_L = \int_0^{\epsilon_y} c_p d\epsilon \tag{11}$$

Eventually, the critical shock wave velocity  $V_s$  of the stabilized shock wave of the ACS can be expressed as:

$$V_s = \sqrt{\frac{2\sigma_{pl}\epsilon_D}{\rho_0}} \tag{12}$$

It can be demonstrated from the Eq. (12) that the critical shock wave velocity is determined by the following three variables: quasi-static platform stress  $\sigma_{pl}$ , densification strain  $\epsilon_D$  and initial density  $\rho_0$  of ACS. Therefore, the impact velocity can be divided into three ranges by trapped velocity and critical shock velocity of the stable shock wave. Similarly, axial impact responses of ACS can also be divided into three intervals. As  $V < V_w$ , the deformation mode of ACS is subject to quasi-static deformation. As  $V_w < V < V_s$ , the response of ACS is within the range of quasi-static deformation and dynamic response. When  $V > V_s$ , the response of ACS is characterized as dynamic response of stable shock wave.

### 6 INFLUENCE OF IMPACT VELOCITIES ON AXIAL IMPACT PERFORMANCE OF ACS

According to Eqs. (11) and (12), three typical impact velocities are chosen as follows:  $V = 5 \text{ m/s} < V_w$ ,  $V_w < V = 20 \text{ m/s} < V_s$ ,  $V = 100 \text{ m/s} > V_s$ . Next, the axial impact performance and impact deformation mode of FSCS, ROH and RHH will be further analyzed to explore the effects of various impact velocities (5 m/s, 20 m/s and 100 m/s) on axial impact performances of the three ACS.

Through FE simulation analysis, the stress-strain curves and unit volume energy absorption-strain curves of the three ACS are achieved with the impact velocity of 5 m/s, as exhibited in Fig. 13 and Fig. 14 below.

As indicated in Fig. 13, as the impact velocity reaches 5 m/s, the platform stress of FSCS in platform stress area proves to be less than that of the RHH, but greater than that of the ROH. It can be drawn from Fig. 14 that the unit volume energy absorption of FSCS keeps less than that of RHH. For FSCS, the existence of platform stress-enhancement area greatly improves the performance of energy absorption, and its effective unit volume energy absorption keeps larger than those of ROH and RHH.

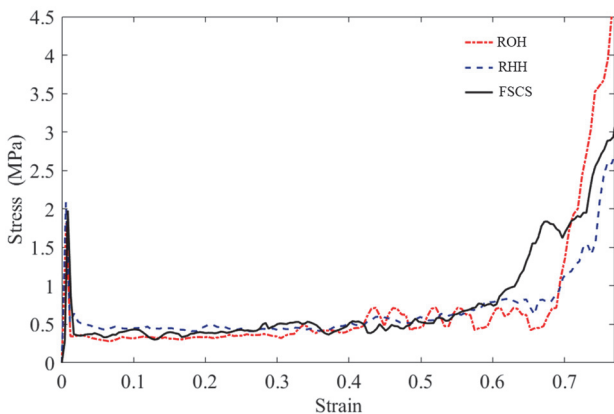


Figure 13 Stress-strain curves of the three ACS with the impact velocity of 5 m/s

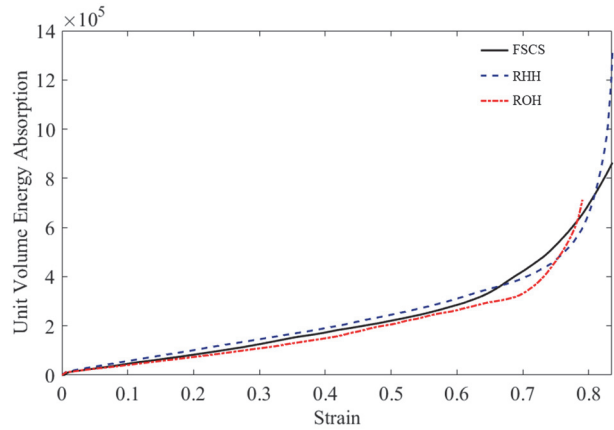
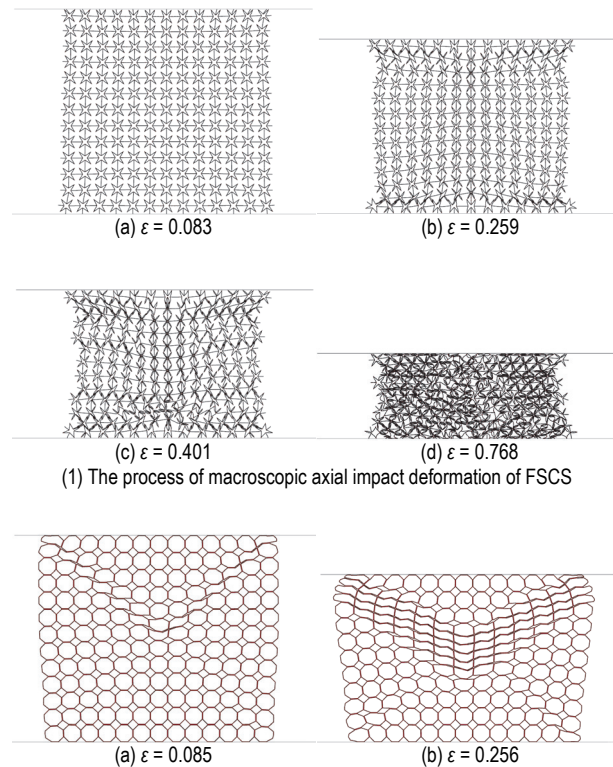


Figure 14 Unit volume energy absorption of the three ACS with the impact velocity of 5 m/s

Similarly, the macroscopic axial impact deformation processes of the three ACS at the same impact velocity of 5 m/s but various compression strains  $\epsilon$  can also be presented in Fig. 15.

It is apparent from Fig. 15 (1) that as the compression strain  $\epsilon$  gradually increases, the FSCS continues to shrink to the middle as a whole, presenting an obvious NPR characteristic. The existence of NPR characteristic makes a platform stress-enhancement area appear at the later stage of platform stress area, which effectively improves collision energy absorption performance of FSCS. Fig. 15 (2) and Fig. 15 (3) indicate that RHH and ROH present "compression-expansion" PPR characteristic under low velocity of 5 m/s. After the final compression and compaction, the RHH and ROH immediately enter into densification strain area without platform stress-enhancement region, and the ROH shows a "V" shape deformation mode, while the RHH presents an "X" shape deformation mode, which illustrates those different forms of ACS present various macro deformation patterns, which in turn affects the overall performance of ACS.



(1) The process of macroscopic axial impact deformation of FSCS

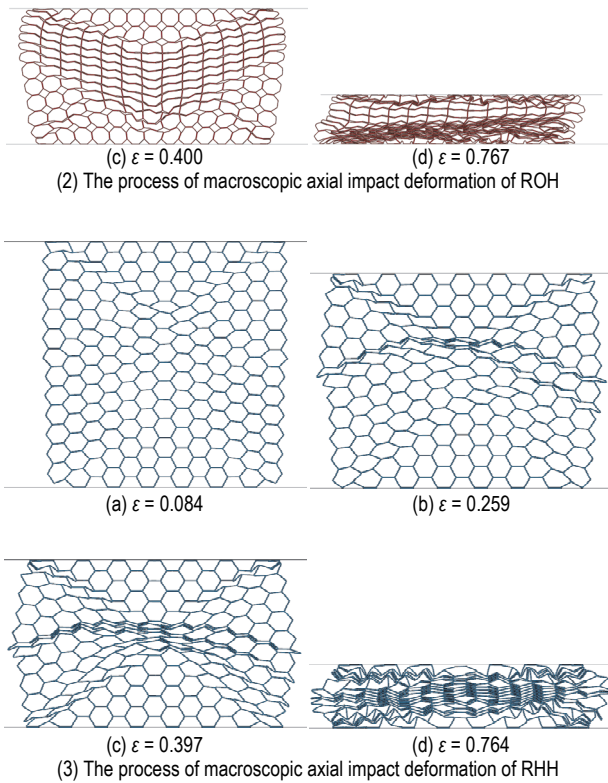


Figure 15 The macroscopic axial impact processes of the three types of ACS with the impact velocity of 5 m/s

Likewise, the stress-strain curves and unit volume energy absorption-strain curves of the three types of ACS at impact velocity of 20 m/s can be obtained either, as illustrated in Fig. 16 and Fig. 17.

In the same way, as the impact velocity keeps 20 m/s, the platform stress of FSCS is significantly higher than those of RHH and ROH, which suggests that the platform stress of FSCS proves more sensitive to the magnitude of impact velocity. Compared with other two ACS, the inertial effects of FSCS caused by the increase of impact velocity are more obvious, and there exists a platform stress-enhancing area which keeps a long time before entering the densification area that can effectively enhance energy absorption performance. Since the stress held by FSCS is more excessive than those of the other two honeycomb structures under the same strain in the platform stress area hence the unit volume energy absorption of FSCS keeps always larger than those of RHH and ROH.

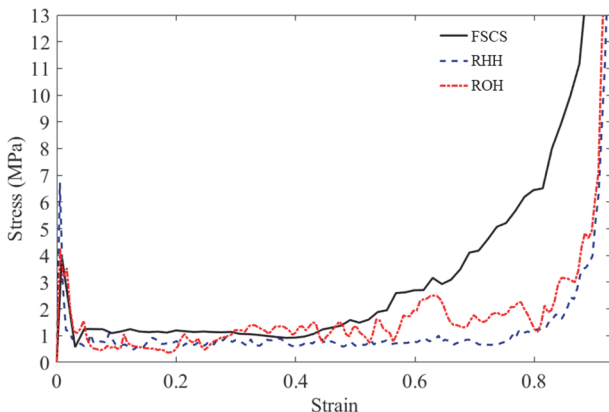


Figure 16 Stress-strain curves of the three ACS with the impact velocity of 20 m/s

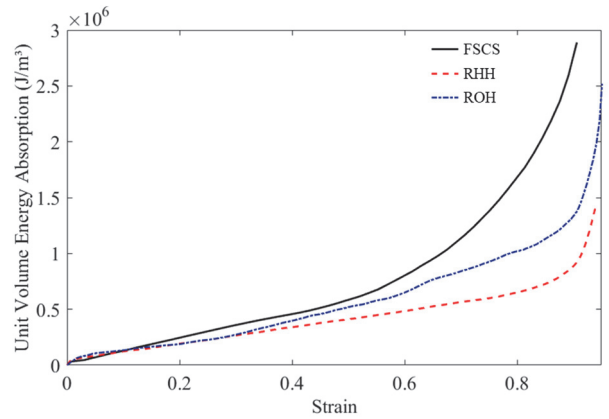
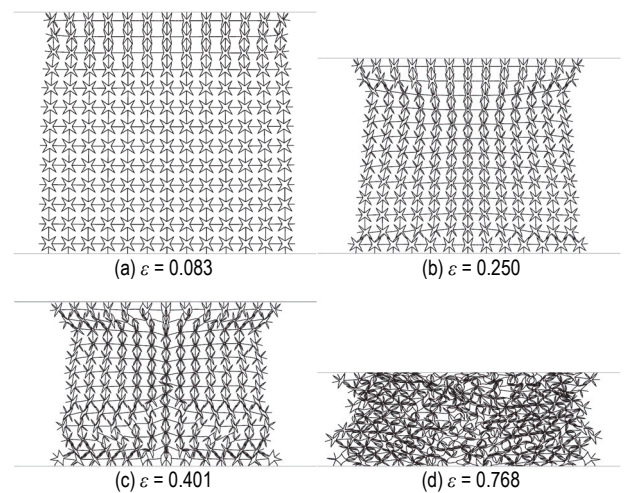


Figure 17 Unit volume energy absorption of the three ACS with the impact velocity of 20 m/s

Similarly, the macroscopic dynamic deformation process of the three types of ACS can also be acquired at impact velocity of 20 m/s, as shown in Fig. 18 above, from which the macroscopic deformation modes of three ACS can be apparently observed. Fig. 18 demonstrates the specific dynamic impact process of the three ACS under the same impact velocity  $V = 20$  m/s and various compression strain. Conclusions can be drawn that as the rigid wall begins to impact the FSCS, the deformation becomes localized and cell layers near the impact end begin to deform. As the compression process continues, the stress wave reaches the bottom. Due to the limitation of the degree of freedom of the bottom cells, the impact end and the bottom end of FSCS deform simultaneously. As the stress that unit cell wall bears exceeds the yield limit, the deformation extends towards the middle, and the cell shrinks toward the central axis parallel to the impact direction. The cells gradually fail, and the cell walls fit together steadily, and the whole FSCS shrinks toward the center, exhibiting more pronounced NPR characteristic. As FSCS is gradually compressed and compacted, it enters into densification area, and the stress rises sharply, with the slope of stress-strain curve increasing greatly among which, the ROH and RHH both reveal PPR characteristic of compression-expansion. According to the corresponding macroscopic dynamic deformation processes, the cells of ROH gradually collapse from the top impact end during the compression process, presenting a macroscopic V-shaped deformation pattern, and the ROH presents a V-shaped deformation mode until it is compacted tightly.



(1) The macroscopic dynamic deformation processes of FSCS

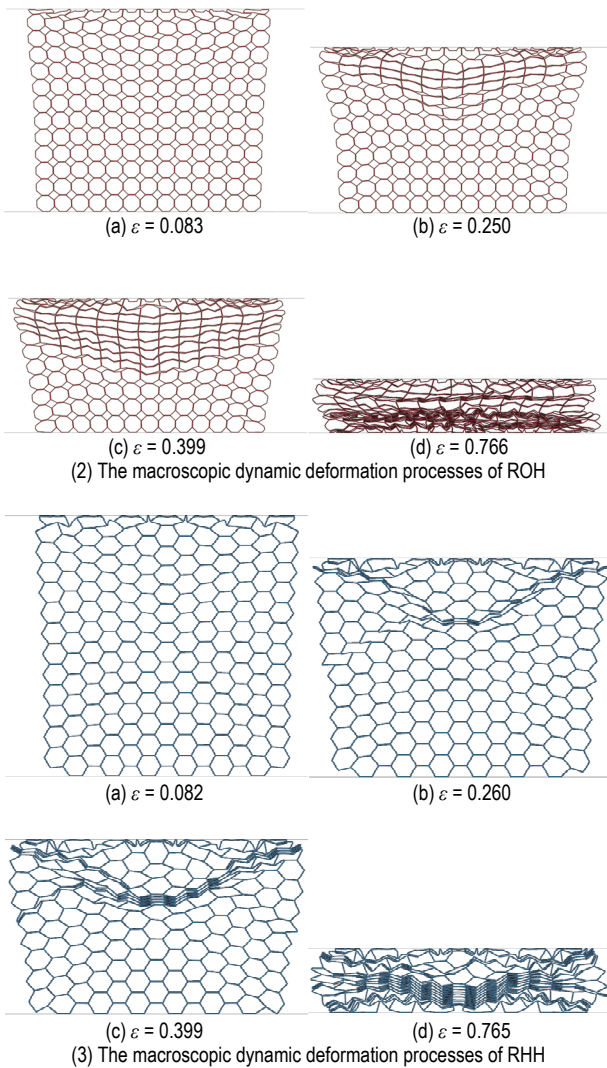


Figure 18 Dynamic impact processes of the three types of ACS with the impact velocity of 20 m/s

Likewise, stress-strain curves and unit volume energy absorption curves of the three types of ACS at the same impact velocity of 100 m/s can be obtained, as shown in Fig. 19 and Fig. 20 respectively.

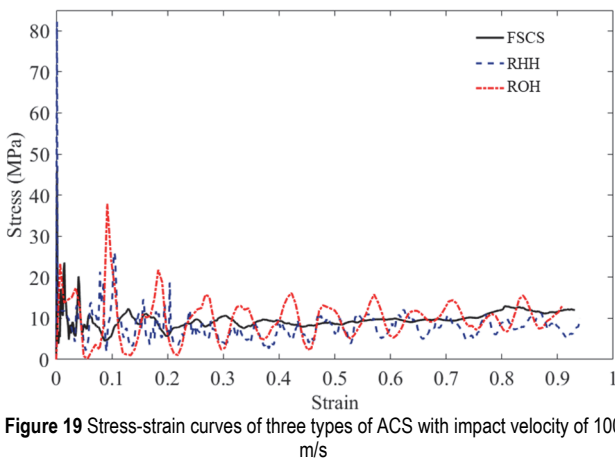


Figure 19 Stress-strain curves of three types of ACS with impact velocity of 100 m/s

According to Fig. 19, the platform stress of FSCS stays between those of RHH and ROH at the initial stage of compression, that is, the platform stress of FSCS is larger than that of the RHH, while less than that of the ROH. It also can be seen from Fig. 20 that the effective unit volume

energy absorption of the FSCS is larger than that of the RHH, while smaller than that of ROH. For the impact energy absorption, the FSCS proves no longer better than the RHH and ROH as the impact velocities are set to 5 m/s and 20 m/s, respectively. In addition, compared with the stress-strain curves with the impact velocities of 5 m/s and 20 m/s, the entry of the three types of ACS into the dense region lags behind, and there exists no obvious densification area before complete compaction, and the FSCS has no platform stress enhancement area.

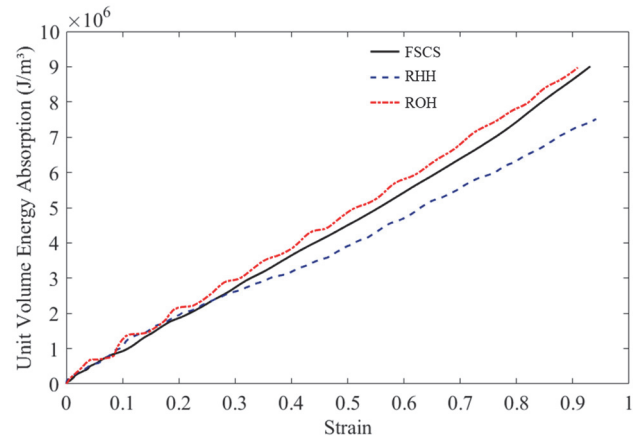


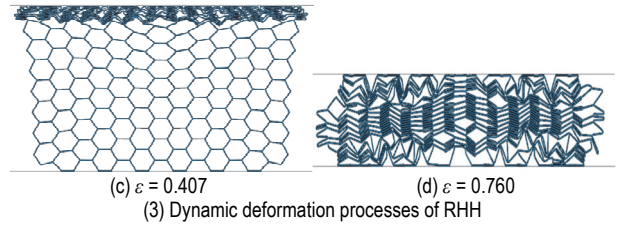
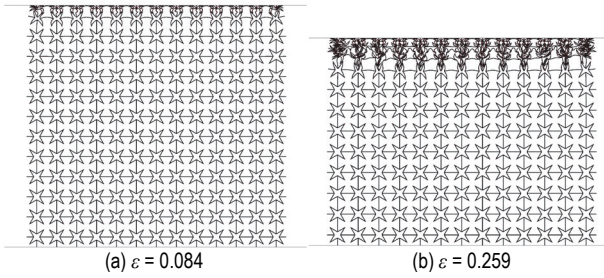
Figure 20 Unit volume energy absorption of three types of ACS with impact velocity of 100 m/s

Similarly, the dynamic impact processes of the three ACS at the same impact velocity of 100 m/s are exhibited in Fig. 21.

It is demonstrated from Fig. 21 that the FSCS absorbs energy through deformation mode of layer collapse without NPR effect of compression-shrinkage. Therefore, there no longer exists platform stress-enhancement area. Additionally, the cells of ROH and RHH are collapsed layer by layer from the impact end, no longer emerging "V" or "X" deformation pattern.

Based on the above-mentioned, it is precisely because of the compressive-shrinkage NPR characteristic of FSCS that leads to appearance of plateau stress-enhancement area in stress-strain curve, with the result of better advantages in unit volume energy absorption than those of ROH and RHH. The reasons can be explained by the following two deformation diagrams at various compression strain stages. As can be seen from Fig. 22 under the impact velocity of 20 m/s and compressive strain  $\epsilon = 0.233$ , as the FSCS is subjected to axial compression load, it demonstrates overall compression-shrink phenomenon that the torsion and bending deformations of cellular walls can effectively absorb the impact energy during the deformation process. With the increment of the compression strain, FSCS shrinks towards the center and leads to connection between cell walls until perfectly fit; afterwards, new structural supports for each other take shape. In addition, the angle between the upper and lower four inner re-entrant edges and the vertical reinforcing bars becomes smaller, while the angle between the left and right four re-entrant edges and the horizontal reinforcing bars becomes larger, and that causes axial deformation of re-entrant cell wall to increase gradually during the compression process, as exhibited in Fig. 23. For slender rods such as re-entrant cell wall, its axial deformation stiffness far outstrips the bending

deformation stiffness. Hence, as FSCS continues to shrink toward the center, the stress on the rigid wall at the impact end increases rapidly, generating platform stress-enhancing area which can improve energy absorption apparently. Whereas, as for RHH and ROH, the angle between the cell walls and the horizontal direction becomes gradually smaller due to their PPR characteristic, the axial deformation component of cell wall does not increase, and no platform stress-enhancement area is formed.



(3) Dynamic deformation processes of RHH  
**Figure 21** Dynamic impact processes of the three types of ACS with the impact velocity of 100 m/s

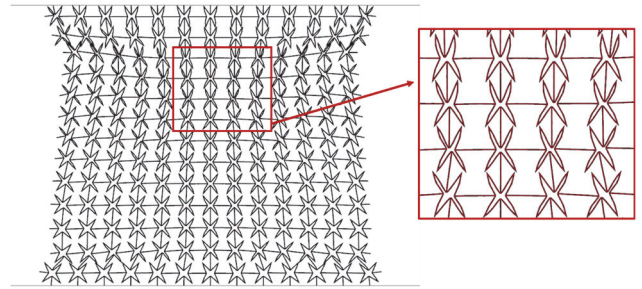
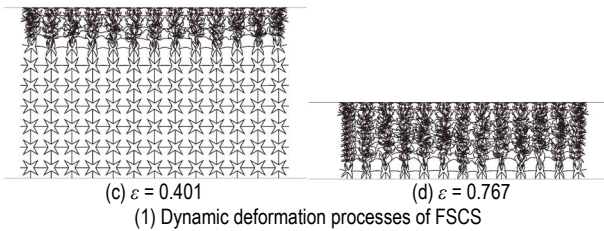


**Figure 22** Deformation mode of FSCS under compression strain  $\varepsilon = 0.233$  with the impact velocity of 20 m/s

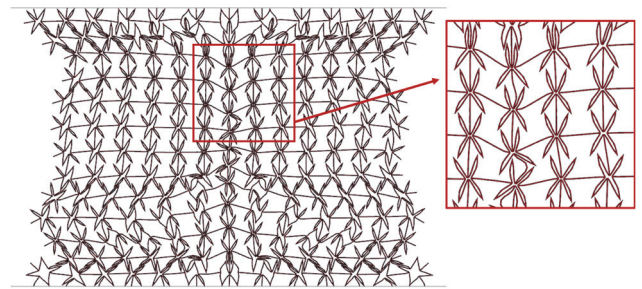
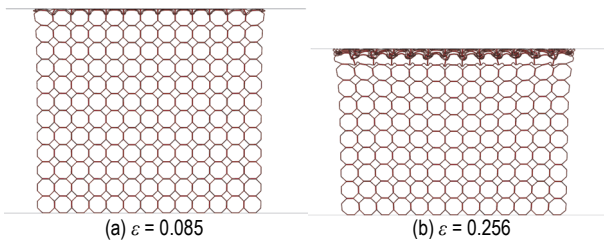
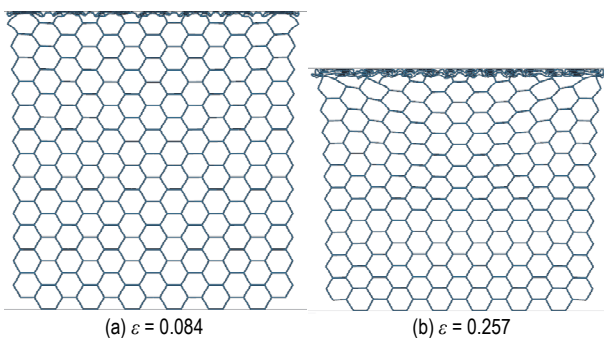
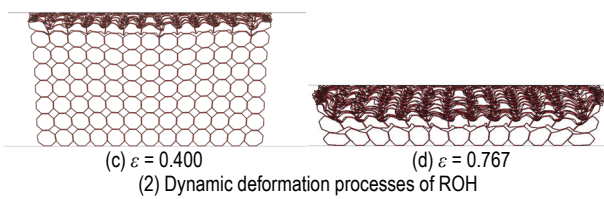


**Figure 23** Deformation mode of FSCS under compression strain  $\varepsilon = 0.434$  with the impact velocity of 20 m/s



Simultaneously, the reasons why the unit cell response under various impact velocities affects the macroscopic deformation pattern of the ACS can also be derived by comparing the deformation modes of the three ACS. As  $V = 5 \text{ m/s} < V_W$ , the three ACS all display a uniform deformation similar to quasi-static deformation mode. The FSCS is possessed with NPR characteristic. This is because when the impact velocity is less than trapped velocity, the propagation of stress keeps faster than the deformation of macro-structure, and the cells deform synchronously, exhibiting a "uniform" deformation mode as a whole. Platform stress area emerges as the stress exceeds the yield limit of cell wall, while the cell walls of FSCS will undergo torsion-bending deformation, leading to the shrinkage of FSCS to the central axis of the cells which are parallel to impact direction, and the three ACS produce a dense strain with the increment of compression.

As the impact velocity climbs to 20 m/s, stresses no longer propagate faster than deformations in the three ACS. The cells which close to the impact end are the first to bear the collapse while others are gradually collapsed owing to inertia effects. Hence, under the impact load  $V = 20 \text{ m/s}$ , the RHH and the ROH manifest a steady transition from the impact end to the fixed end. However, at the same time, the strain of each layer of cells decreases from the impact end to the bottom end layer by layer due to the propagation of stress waves. Nevertheless, the stress

waves propagate faster in FSCS than that in other two honeycombs which results in the local deformation of FSCS at the impact end and the stress wave arrives at the bottom side with the increase of stress. Afterwards, deformation of FSCS starts to propagate from the impact end and bottom end to the middle at the same time owing to the limitation of the degrees of freedom of bottom end. As the stress on the walls of the middle cells exceeds its yield limitation, the re-entrant octagon cells shrink toward the central axis parallel to the impact direction and the structure exhibits NPR characteristic. Similarly, the three types of ACS enter the densification area and dense strains come up as they are gradually compressed and compacted.

The propagation speed of stress waves is basically the same as that of deformation as the impact velocity is set to  $V = 100 \text{ m/s} > V_s$ , and the deformations of the three sorts of ACS all enter the local deformation mode completely, namely, folded deformation pattern. Based on one-dimensional shock wave theory, yield strain occurs where the stress wave propagates. Yet in other regions where the wave does not propagate, the stress proves still too small to induce the yield of cell wall. Therefore, the three ACS are collapsed layer by layer at the impact velocity of 100 m/s. ACS will not enter the dense area so dense strain cannot occur before the last layer is collapsed. In terms of FSCS, the cells are directly crushed where the stress waves travel under the impact load with a velocity of 100 m/s. While, the stress in areas where stress waves do not reach is not enough to raise torsion-bending deformation of cell wall, hence there does not exist NPR effect.

the same strain condition, the re-entrant octagon cells propagated by the stress will undergo torsion-bending deformation, while the cells not propagated by the wave will hardly produce deformation. Compared to the impact load of  $V = 20 \text{ m/s}$ , the deformation of the FSCS under the velocity of 100 m/s turns more localized.

To summarize, FSCS can exhibit compression-shrinkage NPR deformation pattern under the shock load below critical shock velocity  $V_s$ , thus the platform stress-enhancement area comes up, which effectively polishes up its impact energy absorption performance. In general, the impact velocity of vehicle is less than the critical impact velocity  $V_s$  of the stable shock wave, the FSCS discussed herein is possessed with outstanding potentials to be applied to energy absorbers of vehicle.

7 SIZE EFFECTS OF UNIT CELL

The boundary of the ACS discussed herein is assumed to be ideal. As a matter of fact, the mechanical properties of ACS are affected by boundary conditions. Studies have shown that if the macroscopic size of ACS is larger than the size of unit cell and the number of unit cells keeps more as well, the less the effects of undesirable boundary conditions on its mechanical properties, the smaller the error between homogenized equivalent performance models of ACS and the mechanical response of ACS in practical applications [17]. However, it is impossible to adopt infinite number or infinitesimal size of re-entrant octagon cells in engineering applications. Therefore, it is necessary to use FE simulation analysis method to analyze the influences of various layers of cells on their mechanical properties.

The size effect is to fill different numbers of unit cells in the specimen with specific size. Based on the condition that the relative density and the volume of the matrix material of ACS keep equal, the number of unit cells varies along  $X$ -axis and  $Y$ -axis directions by changing the size of unit cell. Assuming that the size of the specimen to be filled is  $L_1 \times L_2 = 750 \times 750 \text{ mm}$ , different numbers of re-entrant octagon cells are filled separately in consideration of equal relative density and equal volume of matrix material. Fig. 25 displays the calculation models of FSCS with different cell layers, in which 2, 3, 4, 5, 6, 7, 8, 9, 10, 11, 12, 13, 14 represent different number of cell layers. As the number of cell layers is 2, it means that there are two re-entrant octagon cells along  $X$  and  $Y$  direction respectively, existing the total number of  $2^2$  cells. As the number of cell layers reaches  $n$ , it means that there are  $n$  re-entrant octagon cells along  $X$  and  $Y$  direction, respectively, and there are totally  $n \times n$  cells.

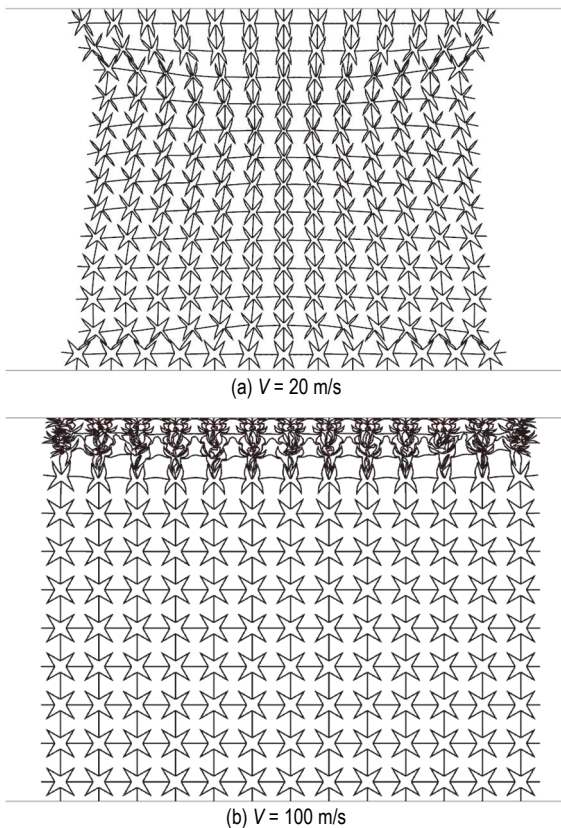
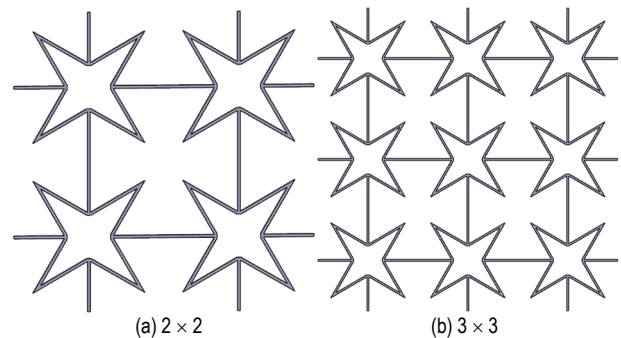


Figure 24 Cellular responses under the same strain with various impact velocities of FSCS

Conclusions can be drawn by analyzing Fig. 24 that under the impact loads of  $V = 20 \text{ m/s}$  and  $V = 100 \text{ m/s}$  with



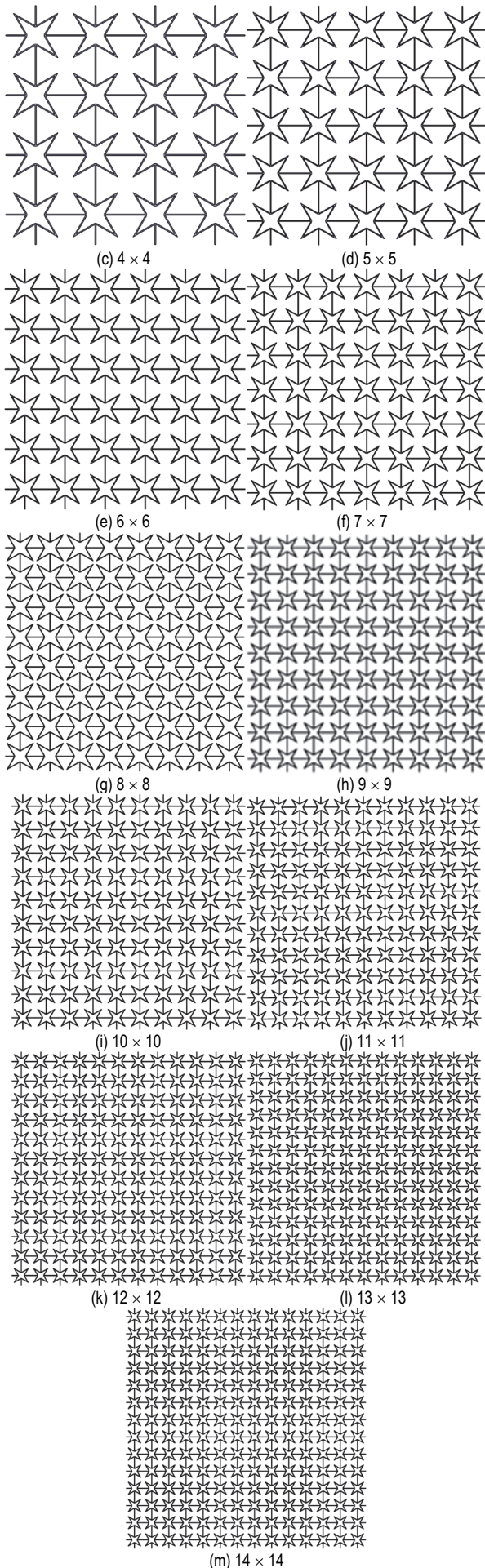


Figure 25 Computational models of FSCS with different cell layers

With the same meshing method and boundary constraint conditions as the FE simulation model established above, the impact velocity of 10 m/s is applied to the impact rigid wall. The relationship curves between the number of layers and platform stress and maximum effective unit volume energy absorption are obtained respectively, as illustrated in Fig. 26 and Fig. 27, respectively. Conclusions can be drawn that with the gradual increase of the number of cell layers, the platform stress of FSCS reveals a gradual increase trend and as the number of cell layers reaches 9 or more, the platform stress of FSCS changes slowly and gradually tends to be stable. It can also be seen from Fig. 27 that as the number of layers increases gradually, the maximum effective unit volume energy absorption of FSCS also presents an increasing trend, as the number of cell layers reaches 9 or more, the maximum effective unit volume energy absorption of the FSCS changes slowly and stabilizes gradually. Therefore, it is necessary to ensure that the number of cell layers is more than or equal to 9 as the FSCS is applied in the design of engineering parts.

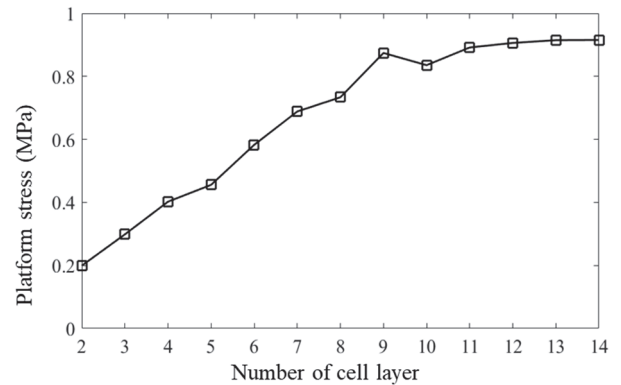


Figure 26 Relations between platform stress and the number of cell layers

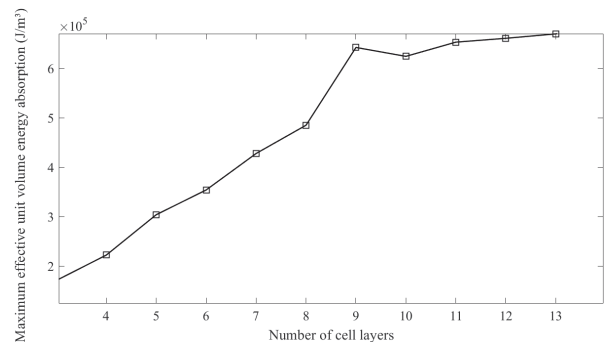


Figure 27 Relations between maximum effective unit volume energy absorption and the number of cell layers

## 8 EXPERIMENTAL STUDIES

In order to verify the accuracy of the FE simulation models, it is necessary to perform quasi-static compression test on the 3D FSCS. The 3D FSCS FE model is shown in Fig. 28, in which the bottom rigid wall is used to fix all the degrees of freedom of bottom cells, and the top rigid wall is employed to impact the 3D FSCS.

The specific structural parameters of the 3D FSCS are listed as follows: in-plane thickness coefficient of reinforced rib is 0.26, in-plane thickness coefficient of re-entrant edge is 0.125, out-of-plane thickness coefficient is

0.26, length coefficient is 1.5, and the re-entrant angle  $\theta$  is  $60^\circ$ , the number of layers is set as 5 along  $X$  and  $Y$  directions, 9 along  $Z$  direction.

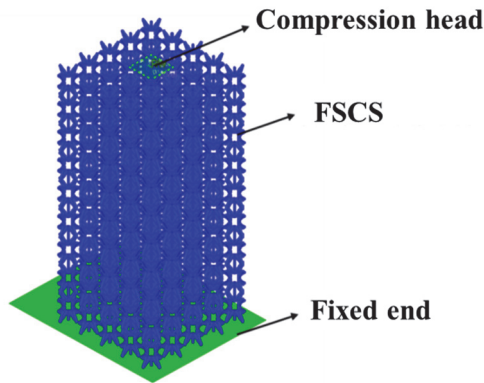


Figure 28 FE model of 3D FSCS

In order to verify the accuracy of the FE simulation model, a quasi-static compression test is required for 3D FSCS. Firstly, the wire cutting process is utilized to process the 3D FSCS sample, 302 stainless steel is adopted as the base material, the bottom end is fixed with rigid wall. Finally, the quasi-static compression test is carried out on the 3D FSCS samples by adopting electronic universal testing machine. Fig. 29 presents the testing machine and 3D FSCS sample.

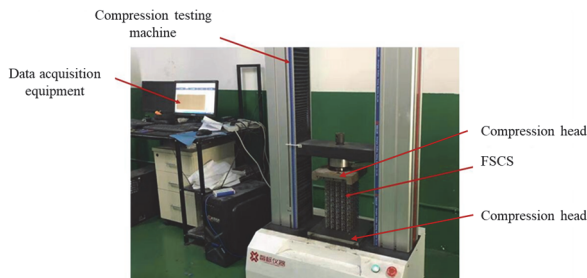


Figure 29 The compression testing machine and the FSCS sample

The compression load speed of the compressor is set as 2 mm/min. Finally, the relation curve between the test force and compression displacement of ACS is obtained through data acquisition device, then the corresponding stress-strain curve can be obtained by calculation. Figure 30 exhibits theoretical predictions of 3D FSCS and the comparison of emulation and testing results. The Poisson's ratio of the FSCS is calculated by measuring and recording the displacement values in all directions, the final test results are shown in Tab. 2.

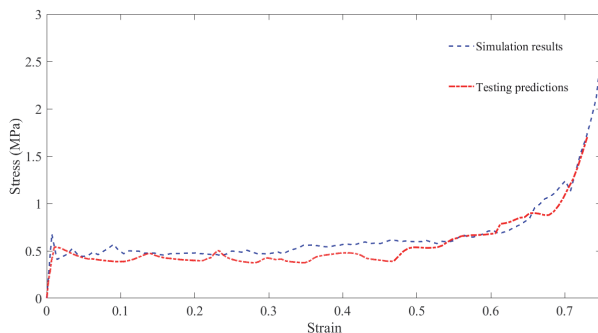


Figure 30 The comparisons of emulation results and testing results

Table 2 Comparisons between simulation results and experimental results of 3D FSCS

Mechanical properties	Testing predictions	Simulation results
Elastic modulus / MPa	55.25	61.22
Platform stress / MPa	0.4217	0.5154
Poisson's ratio	-0.41	-0.525

By comparing the FE simulation result and experimental predictions of FSCS shown in Fig. 30 it can be concluded that the two stress-strain curves prove to have a better agreement. In order to reduce stress concentration, the acute angle in FE model of FSCS is rounded in consideration of actual process, which will make the re-entrant edge of FSCS become shorter and introduce a certain error. In addition, for simulation results are acquired under ideal conditions, the elastic modulus of the FE simulation results under quasi-static compression proves higher. The mechanical performances of testing predictions prove poorer, which attributes to the existence of some micro-cracks, bending and other defects in cutting process of FSCS sample, finally leading to the degradation of performances. Moreover, the existence of friction in test conditions, unsatisfactory boundary conditions and the collapse of local reinforcement during the test make the Poisson's ratio of quasi-static compression test to differ greatly from that of emulation results. Overall, the error between experimental results and FE simulation results is small, which indicates the accuracy of FE simulation model.

## 9 CONCLUSIONS

This work initially puts forward a novel FSCS, relative density theoretical formula of FSCS as well as other two ACS are derived. On this basis, the macro-structural response and micro-deformation patterns of FSCS, ROH and RHH under quasi-static compression and dynamic impact loading with the conditions of equal relative density, equal cell number and equal mass are analyzed through FE simulation method. Through simulation analysis, it can be concluded that FSCS begin to shrink towards the middle as the compression is further strengthened, exhibiting obvious "compression-shrinkage" NPR characteristic. Whereas, the RHH and ROH present opposite characteristic of "compression-expansion" PPR. The corresponding stress-strain curves indicate that stress of FSCS increases evidently earlier than those of the other two on account of its NPR characteristic, which enables the FSCS to gather towards the center so that the bars contact each other earlier to arrange a new support and enter platform stress-enhancement area. While, stresses of the other two ACS increase significantly only when they are compacted. Hence, FSCS prove to exhibit outstanding energy absorption performance compared with the other two ACS.

In addition, the causes are also discussed thoroughly based on macroscopic axial impact deformation processes of the three ACS. Subsequently, size effects of unit cell are also carried out, and results show that as the number of cell layers is more than or equal to 9, platform stress of the FSCS changes slowly and gradually tends to be stable. In order to verify the accuracy of FE simulation models, quasi-static compression test is executed on three-dimensional (3D) FSCS. The results indicate that FE

simulation results prove to agree well with experimental predictions.

The novel FSCS put forward in this article presents prominent energy absorption performance. The results are encouraging in the sense that it offers another potential material for engineers to address the issue and the novel type FSCS with NPR characteristic can be widely promoted and achieve further application in automotive energy absorbers.

## Acknowledgments

This work was sponsored by Natural Science Foundation of Chongqing, China (Grant No. cstc2020jcyj-msxmX0996) and Young Elite Scientists Sponsorship Program by CAST (Grant No. 2021QNRC001).

## 10 REFERENCES

- [1] Qiang, G. A., Whl, A., & Lwb, C. (2020). On the low-velocity impact responses of auxetic double arrowed honeycomb. *Aerospace Science and Technology*, 98. <https://doi.org/10.1016/j.ast.2020.105698>
- [2] Chen, X., Fu, M. H., Li, W. H., & Sheshenin, S. V. (2021). An unusual 3D metamaterial with zero poisson's ratio in partial directions. *Advanced Engineering Materials*. <https://doi.org/10.1002/adem.202001491>
- [3] Wang, Z. G. (2019). Recent advances in novel metallic honeycomb structure. *Composites Part B-engineering*, 166, 731-741. <https://doi.org/10.1016/j.compositesb.2019.02.011>
- [4] Ren, X., Zhang, X. Y., & Xie, Y. M. (2019). Research progress in auxetic materials and structures. *Chinese Journal of Theoretical and Applied Mechanics*, 3(22). <https://doi.org/10.6052/0459-1879-18-381>
- [5] Lee, D. & Shin, S. (2016). Evaluation of Optimized Topology Design of Cross-Formed Structures with a Negative Poisson's Ratio. *Iranian Journal of Science and Technology-transactions of Civil Engineering*, 40(2),109-120. <https://doi.org/10.1007/s40996-016-0016-1>
- [6] Fang, G. D., Yuan, S. G., Meng, S. H., & Liang, J. (2019). Graded negative Poisson's ratio honeycomb structure design and application. *Journal of Sandwich Structures & Materials*, 21(7), 2527-2547. <https://doi.org/10.1177/1099636218755555>
- [7] Lethbridge, Z., Williams, J. J., Walton, R. I., Smith, C. W., Hooper, R. M., & Evans, K. E. (2006). Direct, static measurement of single-crystal Young's moduli of the zeolite natrolite: Comparison with dynamic studies and simulations. *Acta Materialia*, 54(9), 2533-2545. <https://doi.org/10.1016/j.actamat.2006.01.034>
- [8] Rong, Y. A., Wei, L. B., Hua, Y. A., Ji, A., Wh, C., & Zy, A. (2020). Experimental and numerical research on foam filled re-entrant cellular structure with negative poisson's ratio. *Thin-Walled Structures*, 153. <https://doi.org/10.1016/j.tws.2020.106679>
- [9] Lu, Z. X., Li, X., Yang, Z. Y., & Xie, F. (2016). Novel structure with negative poisson's ratio and enhanced young's modulus. *Composite Structures*, 138, 243-252. <https://doi.org/10.1016/j.compstruct.2015.11.036>
- [10] Fu, M. H., Zheng, B. B., & Li, W. H. (2017). A novel chiral three-dimensional material with negative poisson's ratio and the equivalent elastic parameters. *Composite Structures*, 176(sep.), 442-448. <https://doi.org/10.1016/j.compstruct.2017.05.027>
- [11] Shen, J., Ge, J., Xiao, J., & Liang, J. (2020). In-plane impact dynamics of honeycomb structure containing curved reentrant sides with negative poisson's ratio effect. *Mechanics of Advanced Materials and Structures*, (10), 1-9. <https://doi.org/10.1080/15376494.2020.1824285>
- [12] Zhang, X. C., An, L. Q., Ding, H. M., Zhu, X. Y., & El-Rich, M. (2014). The influence of cell micro-structure on the in-plane dynamic crushing of honeycombs with negative poisson's ratio. *Journal of Sandwich Structures and Materials*, 17(1), 26-55. <https://doi.org/10.1177/1099636214554180>
- [13] Qi, C., Jiang, F., Yu, C., & Yang, S. (2019). In-plane crushing response of tetra-chiral honeycombs. *International Journal of Impact Engineering*, 130(Aug.), 247-265. <https://doi.org/10.1016/j.ijimpeng.2019.04.019>
- [14] Zhang, J. & Lu, G. (2020). Dynamic tensile behaviour of re-entrant honeycombs. *International Journal of Impact Engineering*, 139, 103497. <https://doi.org/10.1016/j.ijimpeng.2019.103497>
- [15] Zhang, W., Xu, S., & Zhu, J. (2021). Multi-scale topology optimization method for cyclic symmetric structures. *Chinese Journal of Computational Mechanics*, 38(04), 512-522. <https://doi.org/10.7511/jslx2021057413>
- [16] Aboudi, J. (1984). Elastoplasticity theory for porous materials. *Mechanics of Materials*, 3(1),81-94. [https://doi.org/10.1016/0167-6636\(84\)90015-2](https://doi.org/10.1016/0167-6636(84)90015-2)
- [17] Ypsilantis, K. I., Kazakis, G., & Lagaros, N. D. (2020). Two-scale topology optimization using homogenization theory. *Procedia Manufacturing*, 44, 449-456. <https://doi.org/10.1016/j.promfg.2020.02.271>

## Contact information:

### Ying ZHAO

(Corresponding author)  
College of Engineering and Technology,  
Southwest University,  
No. 2 Tiansheng Road, Beibei District, Chongqing City  
E-mail: 18166893680@163.com

### Yu CHEN

College of Engineering and Technology,  
Southwest University,  
No. 2 Tiansheng Road, Beibei District, Chongqing City  
E-mail: cy18008339390@163.com

### Songchuan ZHENG

College of Engineering and Technology,  
Southwest University,  
No. 2 Tiansheng Road, Beibei District, Chongqing City  
E-mail: zsl19981116@163.com

### Jusan YIN

College of Engineering and Technology,  
Southwest University,  
No. 2 Tiansheng Road, Beibei District, Chongqing City  
E-mail: yjs200109@163.com

### Jinyu SHI

College of Engineering and Technology,  
Southwest University,  
No. 2 Tiansheng Road, Beibei District, Chongqing City  
E-mail: sjy1244502863@126.com

### Yunwu LI

College of Engineering and Technology,  
Southwest University,  
No. 2 Tiansheng Road, Beibei District, Chongqing City  
E-mail: liyw\_swu@163.com